

Tautomerism unveils a self-inhibition mechanism of crystallization

Received: 14 November 2022

Accepted: 9 January 2023

Published online: 02 February 2023

Check for updates

Weiwei Tang^{1,2}, Taimin Yang³, Cristian A. Morales-Rivera⁴, Xi Geng¹, Vijay K. Srirambhatla^{5,6}, Xiang Kang², Vraj P. Chauhan¹, Sungil Hong⁴, Qing Tu⁷, Alastair J. Florence^{5,6}, Huaping Mo⁸, Hector A. Calderon^{9,10}, Christian Kisielowski¹⁰, Francisco C. Robles Hernandez¹¹, Xiaodong Zou³, Giannis Mpourmpakis⁴ & Jeffrey D. Rimer¹✉

Modifiers are commonly used in natural, biological, and synthetic crystallization to tailor the growth of diverse materials. Here, we identify tautomers as a new class of modifiers where the dynamic interconversion between solute and its corresponding tautomer(s) produces native crystal growth inhibitors. The macroscopic and microscopic effects imposed by inhibitor-crystal interactions reveal dual mechanisms of inhibition where tautomer occlusion within crystals that leads to natural bending, tunes elastic modulus, and selectively alters the rate of crystal dissolution. Our study focuses on ammonium urate crystallization and shows that the keto-enol form of urate, which exists as a minor tautomer, is a potent inhibitor that nearly suppresses crystal growth at select solution alkalinity and supersaturation. The generalizability of this phenomenon is demonstrated for two additional tautomers with relevance to biological systems and pharmaceuticals. These findings offer potential routes in crystal engineering to strategically control the mechanical or physico-chemical properties of tautomeric materials.

Modifiers of diverse materials^{1–6} exhibit structures and/or compositions that differ from a solute molecule but often contain similar functional motifs that facilitate molecular recognition for modifier binding to crystal surfaces^{7–9}. Here we examine the intrinsic capability of tautomers^{10–12}, or structural isomers, to operate as crystal growth inhibitors. Molecular tautomers are prevalent in many natural and synthetic crystals^{13–15} where they play a central role in the development of pharmaceutical and biological drugs¹² and materials with diverse

optical¹⁶, magnetic¹⁷, electrical¹⁸, and chemical¹⁹ properties. Tautomerism is a ubiquitous phenomenon in nature widely presented in many small organics¹² and bio-macromolecules¹¹ such as peptides, nucleic acids, and proteins. These naturally forming structural isomers undergo interconversions via intramolecular relocation of atoms, most commonly hydrogens (i.e., prototropic tautomerism²⁰). Tautomer interconversion rates in solution are less rapid than conformers, slightly faster than those of diastereomers (e.g., epimers, anomers),

¹University of Houston, Chemical and Biomolecular Engineering, Houston, TX 77204, USA. ²Tianjin University, School of Chemical Engineering and Technology, State Key Laboratory of Chemical Engineering, The Co-Innovation Center of Chemistry and Chemical Engineering of Tianjin, Tianjin 300072, China. ³Stockholm University, Department of Materials and Environmental Chemistry, SE-106 91 Stockholm, Sweden. ⁴University of Pittsburgh, Chemical and Petroleum Engineering, Pittsburgh, PA 15261, USA. ⁵EPSRC Future Manufacturing Research Hub for Continuous and Manufacturing and Advanced Crystallization (CMAC), University of Strathclyde, Technology and Innovation Centre, 99 George Street, Glasgow G1 1RD Scotland, UK. ⁶Strathclyde Institute of Pharmaceutical and Biomedical Sciences, University of Strathclyde, Glasgow G4 0RE Scotland, UK. ⁷Texas A&M University, Materials Science & Engineering, College Station, TX 77843, USA. ⁸Purdue University, Medicinal Chemistry and Molecular Pharmacology, College of Pharmacy, West Lafayette, IN 47097, USA. ⁹Instituto Politecnico Nacional, ESFM-IPN, Departamento de Física, UPALM Zacatenco, Mexico City CDMX 07338, Mexico. ¹⁰The Molecular Foundry, Lawrence Berkeley National Laboratory, One Cyclotron Rd., Berkeley, CA 94720, USA. ¹¹University of Houston, Mechanical Engineering Technology, Houston, TX 77204, USA. ✉e-mail: jrimer@central.uh.edu

and markedly faster than functional, skeletal, cis-/trans-, enantiomer, or positional isomers^{10,21}. Crystallization of molecules with multiple conformers can lead to polymorphism²², while stereoisomers¹ and anomers^{23,24} can function as crystal growth modifiers that alter crystallization rates and/or morphology. Studies of growth kinetics^{25,26} indicate that the presence of multiple conformers in solution generally does not impact crystal growth²⁷ owing to the rapid rate of conformer exchange prior to solute incorporation into the crystal lattice. Several studies have posited^{28,29} that energetic barriers for conformational exchange (ca. 30–40 kJ/mol) could impact crystallization, but evidence for this effect has been elusive. In the case of tautomers, the exchange between structural isomers typically involves energy barriers greater than 40 kJ/mol where the relatively slow rate of

interconversion¹⁰ is comparable to characteristic timescales of solute incorporation into crystals³⁰. Herein we investigate this effect on the crystallization of ammonium urate (NH₄HU), a prototypical tautomeric compound that is a pathological component of kidney stones^{31,32}.

Results

Crystal structure determination and macroscopic crystallization assays

We first prepared NH₄HU crystals in an alkaline ammonium urate growth solution (pH 11) as a reference condition (control) for crystallization studies and for the purpose of NH₄HU structure determination. In basic media, NH₄HU crystallizes as nanorods (Fig. 1a, b). Three-dimensional electron diffraction (3D ED) was performed at low

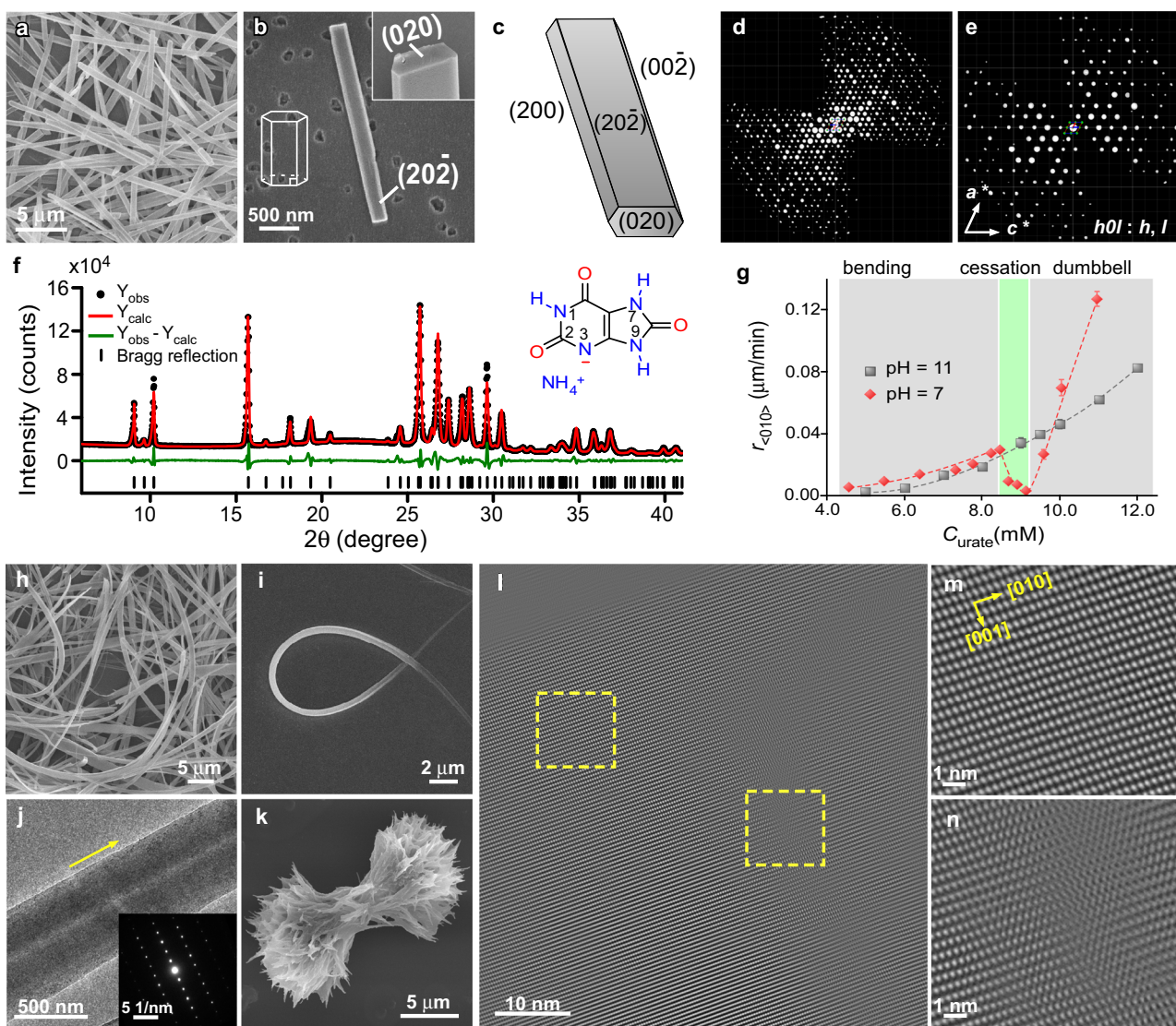


Fig. 1 | Structure and morphology of NH₄HU crystals. **a, b** SEM images of rod-like NH₄HU crystals prepared at pH 11 and 12 mM urate. The inset of panel **b** shows the end face of crystals with a hexagonal cross-section. **c** Schematic diagram of indexed NH₄HU crystal facets. **d** Typical 3D reconstructed reciprocal lattice of a single NH₄HU crystal viewed along the *b*-axis. The crystal facets could be indexed from the 3D ED data, as shown in panel **c**. **e** 2D (*h0l*) slice cut from the reconstructed 3D reciprocal lattice of NH₄HU showing reflection condition *h0l*: *h* = 2*n* and *l* = 2*n*. **f** Pawley profile fitting (red line) of the powder XRD pattern (black dots) with difference plot (green line) of NH₄HU crystals. The black tick marks at the bottom represent the positions of Bragg reflections. Inset: Molecular structure of NH₄HU showing ionization at the nitrogen (N3) site. **g** Microfluidics measurements of macroscopic growth rates along the *b*-direction, $r_{\langle 010 \rangle}$, at pH 11 (control, gray

squares) and pH 7 (red diamonds) as a function of urate concentration. Data are the average measurements of 10 to 15 crystals and error bars span two standard deviations. Dashed lines are interpolated to serve as a guide to the eye. The gray- and green-shaded regions distinguish growth regimes in pH 7 solutions. **h, i** SEM images of NH₄HU crystals prepared at pH 7 and 6–7 mM urate. **j** TEM image showing the straight segment of a bent NH₄HU crystal. Inset: Corresponding SAED pattern revealing the growth orientation along the $\langle 010 \rangle$ direction. Scale bar equals 5 nm⁻¹. **k** SEM image of a crystal prepared at pH 7 and 14 mM urate with a dumbbell-shaped morphology. **l** Filtered TEM image as determined by a low-dose ($4 e^-/\text{\AA}^2$) fractionation technique showing the atomic clusters of the structure (dots in the image) with enlarged images of dashed boxes in panel **l** showing the absence (**m**) and presence (**n**) of defects (see Supplementary Fig. 6).

electron dosage and collected at different tilt angles. The 3D reciprocal lattice of NH_4HU crystal reconstructed from the 3D ED data (Fig. 1d, e, Supplementary Fig. 1a–c, and Supplementary Movie 1) shows that the crystal has a monoclinic space group with $a = 21.385(4) \text{ \AA}$, $b = 3.5300(7) \text{ \AA}$, $c = 20.080(4) \text{ \AA}$, and $\beta = 114.10(3)^\circ$. The short b -axis is along the rod direction and a cross-section (Fig. 1b, inset) with facets is indexed in Fig. 1c. The NH_4HU crystal diffracted to a very high resolution (0.85 \AA) and its structure was solved from the 3D ED data in space group $C2/c$ (Supplementary Table 1). Direct determination of hydrogen positions made it possible to unambiguously identify the correct tautomer species in the crystal, as shown as an inset in Fig. 1f (see also Supplementary Fig. 2). The structure was also refined by powder X-ray diffraction (XRD) data using the Rietveld method (Supplementary Fig. 1d) to confirm the space group. The Pawley fitting profile (Fig. 1f) provided final refined lattice parameters (see Supplementary Table 1 and Supplementary Section 1.3). The asymmetric unit contains equimolar amounts of NH_4^+ and HU^- (Fig. 1f, inset), which was confirmed by carbon, hydrogen, and nitrogen elemental analysis (Supplementary Table 2). These collective analyses provide the first accurate determination of the ammonium urate crystal structure, which differs from those previously proposed in literature³³ (Supplementary Fig. 2), positing different molecular formula.

Uric acid is a polyprotic acid with two dissociation constants ($\text{pK}_a = 5.4$ and 10.3 ; Supplementary Fig. 3a)^{32,34}. The divalent form is the dominant species in highly alkaline media, but 17% of the total urate concentration at pH 11 is monovalent urate HU^- (Supplementary Fig. 3a), the principal component of NH_4HU crystals. The kinetics of bulk NH_4HU growth was measured in situ using microfluidics³⁵ to monitor temporal changes in macroscopic crystal dimension along the b -direction (i.e., length of the rod) at room temperature. The rate of growth, $r_{\langle 010 \rangle}$, was measured in an alkaline medium (pH 11) as a function of the total concentration of urate species, C_{urate} , using a continuous flow rate of supersaturated growth solution (see Methods). The resulting super-linear increase in $r_{\langle 010 \rangle}$ with increasing C_{urate} (Fig. 1g, gray symbols) is typical of classical crystallization^{30,36} where growth occurs by layer generation and spreading (Supplementary Fig. 4d). When the same measurements were performed in a growth medium at neutral conditions (pH 7), where the monovalent form of urate is the most dominant species, there is a deviation in the trend of $r_{\langle 010 \rangle}$ (Fig. 1g, red symbols). At intermediate supersaturation, the rate of growth suddenly decreases to the point of near complete cessation, followed by a rapid increase in crystallization wherein the rate of growth at higher C_{urate} is approximately linear and much faster than $r_{\langle 010 \rangle}$ in the alkaline growth solution. The range of urate concentration where growth cessation occurs is relatively narrow ($8.5 < C_{\text{urate}} < 9.5 \text{ mM}$). At urate concentrations below this range, scanning electron microscopy (SEM) images of NH_4HU crystals extracted from bulk crystallization assays at quiescent conditions reveal natural bending (Fig. 1h), leading to a spaghetti-like morphology (Fig. 1i). Selected area electron diffraction (SAED) patterns (Fig. 1j) and powder XRD (Supplementary Fig. 5) confirm the crystallinity of bent NH_4HU . At concentrations above growth cessation, we observe dendritic growth leading to a dumbbell shape (Fig. 1k) that can evolve into a spherulite-like morphology (Supplementary Fig. 3b). These hierarchical structures mimic the features of crystals extracted from pathological stones^{32,37}, where physiological pH 5–8 matches that of our in vitro experiments. Transmission electron microscope (TEM) images of straight segments in bent crystals (Fig. 1l) and magnified regions (Fig. 1m, n) exhibit remarkable resolution of NH_4HU crystals showing the atomic clusters of the organic crystals as dots. The cluster arrangements clearly show crystalline structural ordering along with the presence of defects (vide infra). The Fourier Transform Filtered images in Fig. 1l–n were obtained by an electron microscope technique that combines the use of rather low doses to preserve the genuine

structure of the sample with a limitation on the number of images (see Supplementary Fig. 6 for unfiltered images).

Microscopic analysis of crystal growth and self-inhibition dynamics

Microscopic evidence of different NH_4HU crystal growth regimes was extracted from in situ atomic force microscopy (AFM) measurements on basal ($20\bar{2}$) crystal surfaces as a function of growth solution alkalinity and urate concentration. Working with a supersaturated growth solution at pH 7 in the regime corresponding to crystal bending ($C_{\text{urate}} = 8.1 \text{ mM}$), we observe the birth and spreading of two-dimensional (2D) islands. Time-resolved images from Supplementary Movie 2 show nuclei (islands I–III in Fig. 2a) that continue to grow with increased imaging time, and a smaller population of islands (IV in Fig. 2a) with radii R that dissolve. The critical radius of 2D nucleation, R_c , is estimated from sequential AFM images by determining a threshold radius above which islands have a higher probability to grow ($R > R_c$), and below which islands are more likely to dissolve ($R < R_c$)^{6,38}. During the growth of new layers, the step velocity in the $\langle 010 \rangle$ direction, $v_{\langle 010 \rangle}$, is much faster than that in the $\langle 101 \rangle$ direction, leading to an anisotropic morphology that mimics the bulk crystal habit. Measurements of step velocity as a function of interstep distance (Supplementary Fig. 7b) reveal a signature profile³⁹ indicative of solute incorporation via a surface diffusion pathway. An unusual observation is the oriented growth of islands wherein steps advance in a direction $[\text{uvw}]$ (Fig. 2a, yellow arrow) at angles $[\text{uvw}] \cap [010]$ between -25° and $+25^\circ$. The distribution of $[\text{uvw}] \cap [101]$ angles for 2D islands, labeled θ_1 in Fig. 2a, has an average value of 81° (Fig. 2b). We also observe highly corrugated steps with large protrusions (dashed circles) that advance at different orientations with a narrower distribution of $[\text{uvw}] \cap [101]$ angles, labeled θ_2 in Fig. 2a, and an average value of 86° (Fig. 2b). The skewed angles of layer advancement at a microscopic level are consistent with macroscopic angles observed in tapered NH_4HU crystals (vide infra).

AFM measurements of step velocity $v_{\langle 010 \rangle}$ as a function of increasing urate concentration (Fig. 2c) reveal an identical trend to macroscopic growth kinetics measured by microfluidics (Fig. 1g), including similar values of C_{urate} corresponding to the sudden drop in step velocity in the regime of growth cessation. In situ AFM measurements were also performed at higher urate concentrations to assess differences in layer growth within the regime where crystal branching leads to dumbbell formation. For these studies, we first stabilized the crystal substrate at a urate concentration (4 mM) slightly above NH_4HU solubility (2.8 mM)³² where we observe a “dead zone” ($v_{\langle 010 \rangle} = 0 \text{ nm/s}$; orange region in Fig. 2c). The latter is consistent with a reported phenomenon in literature where crystal growth modifiers (or impurities) are present in low concentrations^{30,40}, while other factors such as solvent interactions and molecular-scale surface roughness may contribute to the presence of a dead zone^{41,42}. Once the urate concentration is increased to 12 mM, within minutes, we observe the rapid nucleation and growth of highly anisotropic layers (Supplementary Movie 3) comprised of step bunches where unidirectional advancement occurs in either the $[010]$ direction (Fig. 2d, yellow arrow) or $[0\bar{1}0]$ direction (Fig. 2d, white arrow). Time-resolved AFM measurements were conducted at 10 mM urate, where the evolution of step bunch height and rate of advancement could be accurately monitored (Supplementary Movie 4). As shown in Fig. 2e, a step bunch with length $1 \rightarrow 2$ advances in the $[0\bar{1}0]$ direction. Height profiles at periodic imaging times (Fig. 2f) show that step bunch growth is three-dimensional. The initial step bunch height is ca. 2 nm, which is nearly twice the length of a urate molecule ($\sim 0.9 \text{ nm}$). As the step bunch advances unilaterally in length (from 50 to 130 nm over 526 s), the height of the advancing step front increases to 5 nm while the opposite end remains fixed at a height equal to that of the original step bunch.

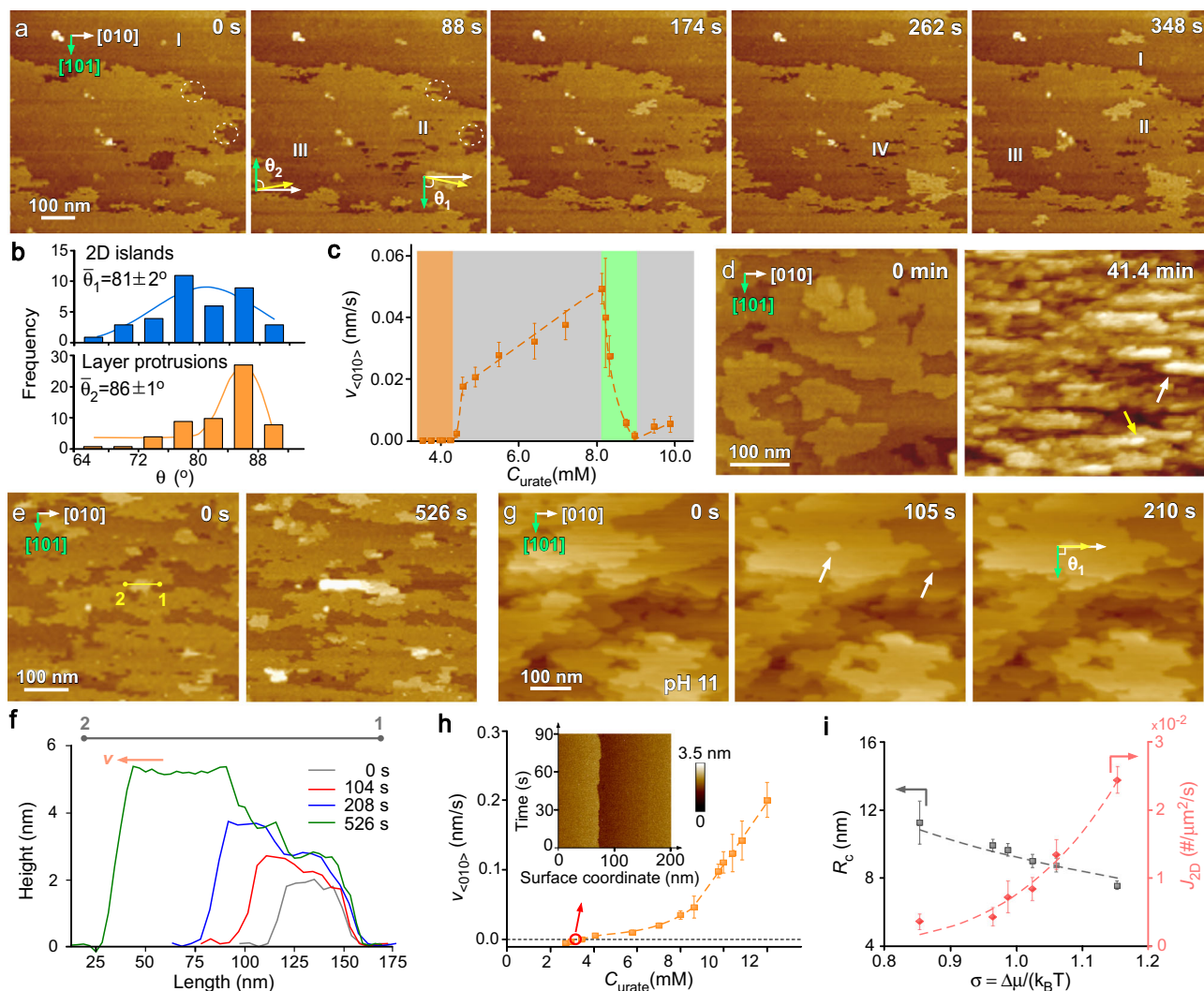


Fig. 2 | Time-resolved AFM images of NH_4HU surface growth. **a** Tapping mode AFM images of (202) surface growth in situ (pH 7 and 8.1 mM urate) extracted from Supplementary Movie 2 show both growing (I–III) and dissolving (IV) islands, and corrugated steps with protrusions (dashed circles). **b** Orientation angles $[\text{uvw}] \cap [101]$ for 2D island (θ_1 , blue) and step protrusion (θ_2 , orange) advancement ($n \geq 40$ measurements of the same sample). **c** Step velocity of layer advancement at pH 7 as a function of urate concentration. The shaded regions indicate a “dead zone” (orange), step growth (gray), and growth cessation (green). Symbols are the average of 10 to 15 measurements and error bars span two standard deviations. **d** Time-elapased images from Supplementary Movie 3 showing the evolution of multilayer step bunches in a growth solution at pH 7 and 12 mM urate ($\sigma = 1.30$). Yellow and white arrows highlight step bunch advancement in the $+b$ and $-b$ directions, respectively. **e** AFM images from Supplementary Movie 4 showing the onset of step bunching in a growth solution at pH 7 and 9.5 mM urate ($\sigma = 1.09$).

f Height profiles of line l_{1-2} in panel e at various time intervals where a single step is 0.9 nm in height. **g** Time-elapased images from Supplementary Movie 5 showing 2D island generation and spreading in a control growth solution (pH 11) with 12 mM urate ($\sigma = 1.15$). White arrows (at 105 s) highlight nuclei that advance in the b direction at angle $\theta_1 = 90^\circ$. **h** Step velocity at pH 11 where symbols are the average of 10 to 15 measurements and error bars span two standard deviations. Inset: In situ AFM kymograph collected with disabled scanning along the y -axis. **i** Dependence of the critical radius of 2D island nucleation R_c and the rate of island nucleation J_{2D} on the crystallization driving force $\sigma = \Delta\mu/k_B T$ at pH 11. Symbols are the average of 25 to 40 measurements and error bars span two standard deviations. The gray dashed line is a plot of the Gibbs–Thomson relation $R_c = \Omega\alpha/\Delta\mu$ with step line tension $\alpha = 247 \pm 4 \text{ mJ m}^{-2}$. The red dashed line is an exponential fit ($J_{2D} \propto \exp(-\Delta G_{2D}^*/RT)$) where ΔG_{2D}^* is the energy barrier of 2D layer nucleation.

AFM measurements of NH_4HU surface growth in alkaline media (pH 11) reveal 2D layer generation and spreading without the abnormalities observed at lower pH. Time-resolved images for 12 mM urate (Supplementary Movie 5) show island nucleation (Fig. 2g, white arrows) where growth occurs preferentially in the $\langle 010 \rangle$ direction (i.e., $\theta_1 = 90^\circ$) and unfinished layers exhibit corrugated edges without noticeable step bunching. The increase in $v_{\langle 010 \rangle}$ with increasing urate concentration (Fig. 2h) exhibits a trend that closely aligns with reported cases of classical crystallization in literature^{30,40} without growth cessation observed at neutral conditions. The solubility of NH_4HU crystals shifts to a slightly higher value (3.4 mM, Supplementary Fig. 4c) in alkaline media, which was confirmed by in situ AFM imaging with disabled scanning along the y -axis where the resulting

kymograph (Fig. 2h, inset) shows a step edge in equilibrium with the solution (i.e. the step neither advances nor recedes with scanning time). Sequential AFM images at each urate concentration were analyzed according to a reported procedure⁶ to obtain the critical radius of 2D island nucleation R_c and the rate of island nucleation J_{2D} (Fig. 2i), which both exhibit trends with increasing supersaturation ($0.85 < \sigma < 1.15$) that are consistent with classical models⁴³.

Confirmation of urate tautomers in growth media

Several observations of NH_4HU crystallization at pH 7 are indicative of growth in the presence of an inhibitor. These include multi-oriented step advancement, the increased density of corrugated step edges, the generation of step bunches, evidence of a dead zone, and the unusual

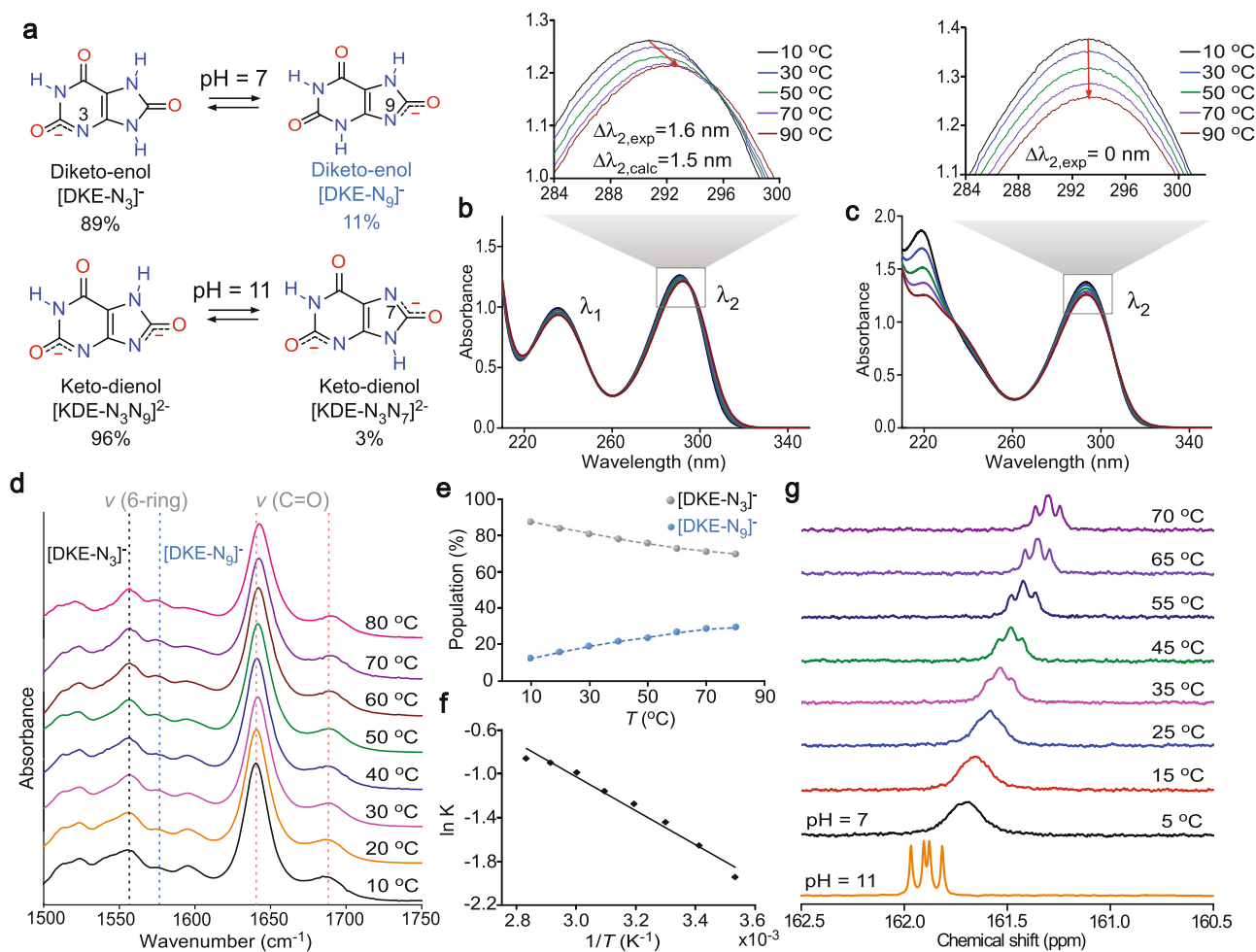


Fig. 3 | Experimental and computational evidence of urate tautomers.

a Chemical equilibrium between urate diketo-enol tautomers at pH 7 and keto-dienol tautomers at pH 11 (control). Percentages of tautomers are based on first-principles (CBS-QB3) calculations at 25 °C on mono and double deprotonated urate tautomers simulating species at pH 7 and pH 11, respectively. **b** Variable-temperature UV-Vis spectra of an aqueous 1 mM urate solution at pH 7. Inset: Bathochromic shift of the absorption peak λ_2 with increasing temperature with maximum peak shifts from the experiment ($\Delta\lambda_{2,\text{exp}}$) and DFT ($\Delta\lambda_{2,\text{calc}}$, Supplementary Fig. 10c). **c** Variable-temperature UV-Vis spectra of a 1 mM urate solution at pH 11. Inset: Absorption peak λ_2 with increasing temperature shows no shift. **d** FTIR spectra of 18 mM urate in D_2O at different temperatures. The asymmetric stretching modes of the six-membered ring show increasing intensity of peaks at 1576 cm^{-1} ($[\text{DKE-N}_9]^-$) relative to 1556 cm^{-1} ($[\text{DKE-N}_3]^-$) with increasing temperature. There is a

concomitant red shift of carbonyl group asymmetric vibration bands (see Supplementary Fig. 11a for IR peak assignments). **e** Population of $[\text{DKE-N}_9]^-$ and $[\text{DKE-N}_3]^-$ tautomers derived from the relative intensity of IR absorption peaks at 1576 and 1556 cm^{-1} . **f** Temperature dependence of the equilibrium constant K at pH 7 between tautomers $[\text{DKE-N}_9]^-$ and $[\text{DKE-N}_3]^-$ determined from the relative intensity of IR peaks at 1556 and 1576 cm^{-1} . **g** Variable-temperature ^{13}C -NMR spectra of 10 mM urate ($2\text{-}^{13}\text{C}, 1,3,7\text{-}^{15}\text{N}_3$ atomic labeled) in 95% (v/v) $\text{H}_2\text{O}/\text{D}_2\text{O}$ at pH 7 comparison with the same concentration at pH 11 (bottom). In neutral solutions, significant peak broadening transitions to gradual peak sharpening with increasing temperature, reflecting the nature of interconversion between tautomers $[\text{DKE-N}_9]^-$ and $[\text{DKE-N}_3]^-$ (Supplementary Fig. 7a and Supplementary Movie 6). The appearance of a doublet-doublet peak is due to the scalar couplings from two adjacent, labeled ^{15}N resonances.

appearance of growth cessation in a narrow range of urate concentration. We hypothesize that all these observations can be correlated to urate tautomerization, wherein the minor tautomer, which is non-native to the crystal structure, functions as a crystal growth inhibitor. Here we use a combination of spectroscopy measurements and first-principles calculations to examine the stability of tautomers in aqueous solutions at pH 7 and 11. Free energy CBS-QB3 calculations at pH 7 and room temperature, including implicit water solvation, predict out of 30 total urate tautomers (Supplementary Fig. 8), only two thermodynamically favorable diketo-enol structures (Fig. 3a): $[\text{DKE-N}_3]^-$ and $[\text{DKE-N}_9]^-$. Based on Boltzmann statistics, these tautomers account for 89 and 11% of the urate population, respectively. Similar calculations at pH 11 reveal one predominant structure, keto-dienol $[\text{KDE-N}_3\text{N}_9]^{2-}$, and a minor tautomer $[\text{KDE-N}_3\text{N}_7]^{2-}$ (Fig. 3a) that account for 96 and 3% of the total urate population, respectively. Nineteen additional structures (Supplementary Fig. 9) collectively account for the remaining 1%.

Boltzmann distributions predict the percentage of minor tautomer at neutral pH increases with temperature; therefore, experimental validation of urate tautomerism was conducted over a range of temperatures between 10 and 90 °C using three separate spectroscopy techniques. UV-Vis spectra at pH 7 (Fig. 3b) exhibit a peak shift from 290 to 291.6 nm ($\Delta\lambda_{2,\text{exp}} = 1.6\text{ nm}$) with increasing temperature, which is nearly equal to the peak shift, $\Delta\lambda_{2,\text{calc}} = 1.5\text{ nm}$, predicted by Density Functional Theory (DFT) calculations (Supplementary Fig. 10c). The UV-Vis spectra at pH 11 (Fig. 3c) display no apparent peak shift owing to the small percentage of minor tautomer $[\text{KDE-N}_3\text{N}_7]^{2-}$. Similar trends are observed in Fourier transform infrared (FTIR) spectra at pH 7 (Fig. 3d), where two signature peaks associated with the carbonyl group around 1640 and 1689 cm^{-1} experience a red shift with increasing temperature. There are also two characteristic peaks associated with asymmetric stretching modes of the 6-membered ring at 1556 and 1576 cm^{-1} for $[\text{DKE-N}_3]^-$ and $[\text{DKE-N}_9]^-$, respectively, that exhibit changes in relative intensity with increasing temperature.

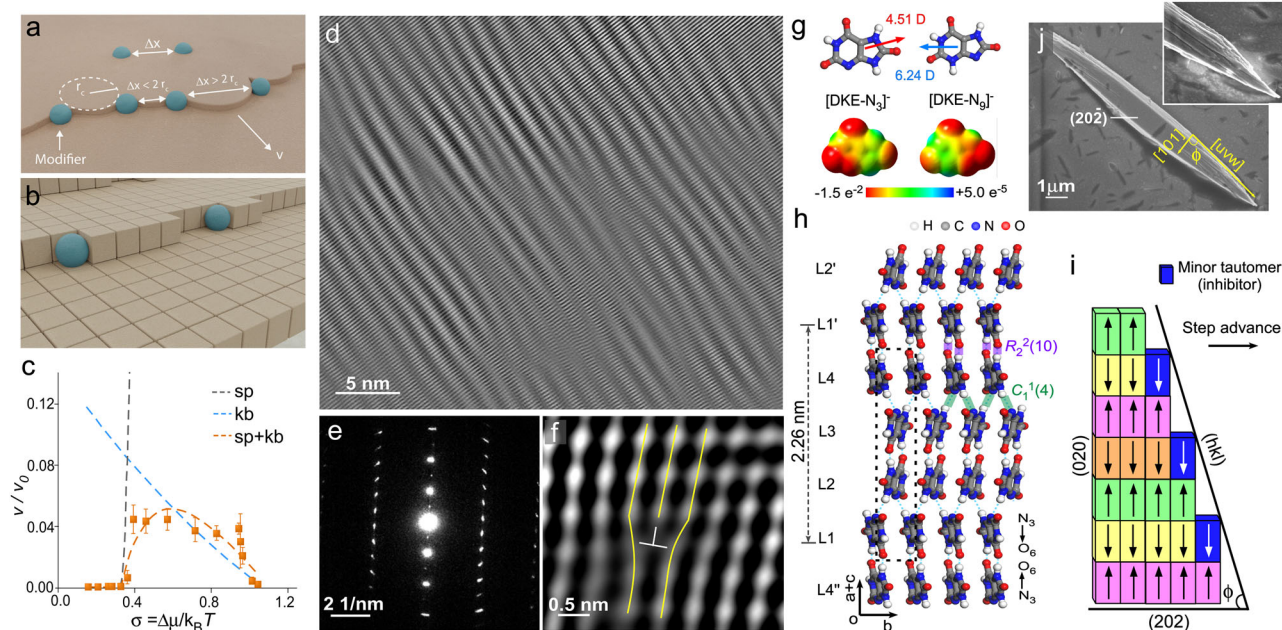


Fig. 4 | Self-inhibition mechanism of the minor tautomer. **a, b** Illustrations of step pinning (**a**) and kink blocking (**b**) mechanisms of growth inhibition⁶. **c** Step velocity v at pH 7 (from Fig. 2c) normalized by v_0 measurements in pH 11 corresponding to growth conditions (control) containing a trace quantity of minor tautomer. Model fits are indicated by dashed lines for step pinning (black), kink blocking (blue), and combined mechanisms (orange). See Supplementary Section 2 for details. **d** TEM image of a bent crystal prepared at pH 7 (see also Supplementary Fig. 6). **e** SAED pattern of a bent crystal showing line broadening. **f** Fourier-filtered high-resolution TEM image showing an edge dislocation. The image is produced by combining ten low-dose experimental images and Fourier filtering to show atomic clusters of the organic crystal. **g** Electrostatic potential of tautomers [DKE-N₃]⁻ and [DKE-N₉]⁻ from DFT calculations showing the difference in charge distribution and dipole moments (arrows with 4.51 and 6.24 Debye, respectively). **h** Molecular packing in the NH₄HU crystal structure viewed on the (202) plane. The unit

cell (dashed box) contains four distinct layers (L1 to L4) differing by their orientation (arrows). Key intermolecular interactions include strong amide-amide hydrogen bonds (purple, $R_2^2(10)$, $d_{N...O} = 2.670 \text{ \AA}$, $\theta_{NH...O} = 159.13^\circ$) forming urate dimer and amine-nitrogen hydrogen-bonding chains (green, $C_1^1(4)$, $d_{N...N} = 2.944 \text{ \AA}$, $\theta_{NH...N} = 165.86^\circ$) connecting urate dimers. Ammonium ions are omitted for clarity. **i** Idealized binding of minor tautomer [DKE-N₉]⁻ to (020) step edge sites via $R_2^2(10)$ hydrogen-bonding interactions. Tautomer binding to only L1 or L3 kink sites would produce a vicinal surface with angles ($\phi = 73 - 90^\circ$, Supplementary Fig. 12f) that are consistent with surface layer angles θ_2 in AFM images (Fig. 2b) and tapering angles ϕ in SEM images. **j** SEM image of a tapered NH₄HU crystal prepared in pH 7 growth solution with 6 mM urate ($\sigma = 1.0$). Inset: Enlarged image of a tapered crystal end where angles $\phi = [uvw] \cap [101]$ span from 72 to 90° (Supplementary Fig. 12c). Measurements of 50 crystals yield an average $\phi = 86 \pm 1^\circ$.

The ratio of FTIR peak intensities for the 6-rings was used to extract the fraction of diketo-enol tautomers as a function of temperature (Fig. 3e) and the corresponding equilibrium constant K (Fig. 3f), which exhibits the expected exponential dependence on temperature, $K \propto \exp(-\Delta H/RT)$ ⁴⁴. The estimated enthalpy of urate tautomerism ΔH ($12.9 \pm 0.8 \text{ kJ mol}^{-1}$) is within the range of reported values ($\Delta H = 7-26 \text{ kJ mol}^{-1}$) for other organic tautomers in literature⁴⁵.

The existence of urate tautomers was also confirmed by variable-temperature solution ¹³C-NMR spectroscopy. As shown in Fig. 3g, the ¹³C-NMR spectrum at pH 11 contains a sharp doublet-doublet peak suggesting the absence of the minor tautomer in contrast to the broad peak observed at pH 7 owing to the presence of [DKE-N₉]⁻. With an increasing temperature of the neutral solution, there is a shift from a single broad peak to a doublet-doublet peak that retains a small degree of peak broadening. These measurements reflect the kinetics of interconversion between [DKE-N₃]⁻ and [DKE-N₉]⁻ tautomers, in agreement with DFT calculations indicating an activation barrier of 73.3 kJ mol^{-1} at 25°C (Supplementary Fig. 7a and Supplementary Movie 6). This indicates a major-minor tautomer exchange rate on the order of milliseconds (Supplementary Table 3), which is within the NMR detection limit, thus explaining why peak broadening is more pronounced at a lower temperature. Collectively, spectroscopy experiments and DFT calculations confirm that growth solutions at pH 11 contain a single urate tautomer, whereas solutions at pH 7 contain a major tautomer with a structure identical to that of urate in the NH₄HU crystal structure and a minor tautomer that we posit is a native crystal growth inhibitor.

Mechanism of self-inhibition by the minor tautomer

There are two common mechanisms of crystal growth inhibition: step pinning (Fig. 4a) and kink blocking (Fig. 4b). Step pinning occurs when modifiers adsorb on terraces or step edges and impose a surface tension on the advancing layer when two adsorbed species are separated by a distance Δx smaller than the critical radius of curvature R_c for the step. Kink blocking involves modifier adsorption to kink sites, which are the most favorable for solute incorporation. Neither inhibitor model (Fig. 4c) alone can capture the step velocity profile at neutral pH measured by AFM; however, the experimental data can be fitted using a combination of both mechanisms (Fig. 4c, dashed orange line), indicating the inhibitor [DKE-N₉]⁻ operates by a dual mode of action. This behavior deviates from reported cases involving a binary combination of inhibitors where each acting by a different mechanism results in antagonistic cooperativity⁶. Here the dual effects of the single inhibitor are synergistic, which suggests kink blockers do not significantly lower the line tension of advancing layers. Slight differences between the experiment and model fit (Fig. 4c) suggest additional factors contribute to growth cessation, such as strain imposed by minor tautomer [DKE-N₉]⁻ occlusion within the crystal that is not accounted for in either kink blocking or step pinning mechanisms. Evidence of tautomer occlusion can be inferred from TEM images of NH₄HU crystals prepared at pH 7, showing irregularities in the crystal structure (Fig. 4d) and SAED patterns (Fig. 4e) with diffuse scattering. High magnification TEM images show numerous dislocations (Fig. 4f) that are responsible for the natural bending (Fig. 1h) and branching of dumbbell-shaped crystals (Fig. 1k) at low and high urate

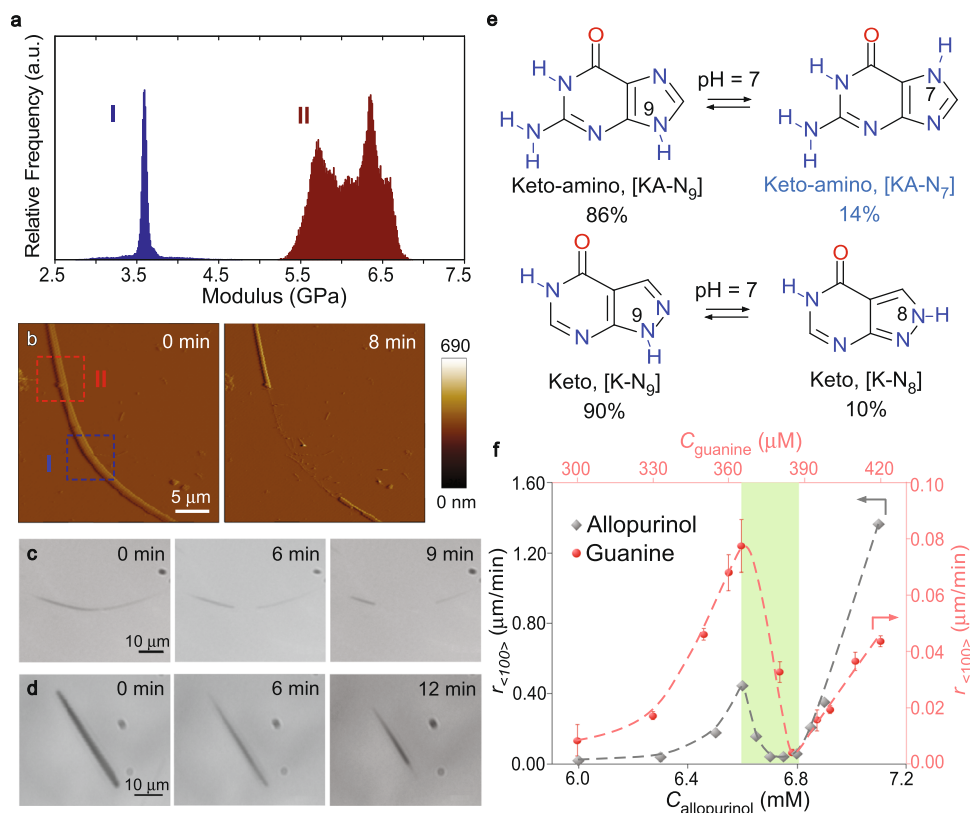


Fig. 5 | Impact of minor tautomers on crystal properties. **a** Elastic modulus of NH_4HU crystals prepared at pH 7 using contact resonance AFM. Data compare regions marked in panel **b** with relatively high (I) and low (II) defect density. **b** Time-elapsed AFM images of an NH_4HU crystal prepared at pH 7 during in situ dissolution in DI water. **c** Snapshots from Supplementary Movie 7 showing the dissolution of NH_4HU crystals prepared at pH 7 in a microfluidics device. Images were collected over 18 min in DI water. **d** Snapshots from Supplementary Movie 8 showing the dissolution of an NH_4HU crystal prepared at pH 11 in a microfluidics device. Images were collected over 36 min. **e** Chemical equilibrium between guanine (top) and

allopurinol (bottom) at pH 7. Percentages of tautomers are based on first-principles (CBS-QB3) calculations at 25 °C (see Supplementary Figs. 13, 14). **f** Microfluidics measurements of macroscopic growth rates at pH 7 along the $\langle 100 \rangle$ direction for guanine (red) and the $\langle 100 \rangle$ direction for allopurinol (grey) as a function of their respective solute concentrations. Data were the average measurements of more than 15 crystals and error bars span two standard deviations. Dashed lines are interpolated to serve as a guide to the eye. The green-shaded region corresponds to growth cessation.

concentrations, respectively. In contrast, TEM images and SAED patterns of NH_4HU crystals prepared at pH 11 contain few defects (Supplementary Fig. 6g) owing to trace quantities of the minor tautomer, which results in crystal growth without noticeable inhibition.

Comparison of the electrostatic potential of major and minor tautomers (Fig. 4g) reveals a delocalization of negative charge that leaves one-half of the molecule with similar molecular recognition (i.e., unhindered binding to crystal surfaces) and the positioning of negative charge that limits $[\text{DKE-N}_9]^-$ interaction with NH_4HU crystal surfaces. Notably, the inhibitor cannot bind to all kink sites equivalently owing to steric hindrance when the negatively-charged segment is oriented directly into the crystal surface, thus breaking the hydrogen-bonding of the crystal structure. The unit cell of NH_4HU (Fig. 4h, dashed box) is comprised of four distinct layers in the $[101]$ direction, labeled L1 to L4, where the orientation of urate molecules and interstitial hydrogen-bonding between layers (Fig. 4h, dashed lines) are distinct. As illustrated in Fig. 4i, this suggests the minor tautomer $[\text{DKE-N}_9]^-$ can only bind to every other layer when the negatively-charged group is oriented away from the step site. This binding motif is analogous to that observed for L-cystine crystals⁴⁶ where symmetric and asymmetric modifiers were shown to exhibit distinct binding modes. Notably, the inhibitor L-cystine methyl ester, which is an asymmetrical modification of solute L-cystine, resulted in tapered crystals. Here we observe a similar effect for NH_4HU crystallization where the asymmetry imposed by negative charges in the two tautomers yields tapered crystals (Fig. 4j) with a tapering angle ϕ that varies between 72 and 90°,

consistent with conceptual models of vicinal surfaces with high to low inhibitor coverage on NH_4HU crystals (Supplementary Fig. 12f). This also agrees with AFM measurements of 2D island and layer protrusion advancement at angles $\theta_1 = 81 \pm 2^\circ$ and $\theta_2 = 86 \pm 1^\circ$ (Fig. 2b), which have average values that lie within the range of macroscopic tapering ($\phi = 86 \pm 1^\circ$) measured from SEM images (see also Supplementary Fig. 12c).

Impact of minor tautomers on crystal properties

The occlusion of minor tautomer as defects impacts the physical properties of NH_4HU crystals prepared at pH 7. AFM nanomechanical characterization reveals that crystal segments containing a high percentage of defects (Fig. 5a, region I) have a lower elastic modulus compared to segments containing fewer defects (Fig. 5a, region II). These differences in mechanical properties impact the relative rates of crystal dissolution. For instance, in situ AFM (Fig. 5b) and microfluidic (Fig. 5c) dissolution measurements in deionized (DI) water reveal inhomogeneous dissolution where segments with high defect density dissolve faster. Similar measurements with less defective crystals prepared at pH 11 (Fig. 5d) reveal homogeneous dissolution. The ability to selectively control physicochemical properties by defect engineering has practical implications for applications such as pharmaceuticals, where dissolution is crucial for oral bioavailability. To assess the broader applicability of our findings, we examined two additional tautomeric compounds (Fig. 5e). The first is allopurinol, an anti-gout drug^{15,47} exhibiting major and minor tautomers at neutral

conditions (Supplementary Fig. 14). Microfluidic measurements of allopurinol crystallization show a trend of growth cessation (Fig. 5f) that is similar to that of urate (Fig. 1g). The second molecule tested is guanine, which is a biogenic crystal widely distributed in animal coloration and visual systems^{13,48,49}. Guanine exists in two tautomeric forms (Fig. 5e) and has an identical region of growth cessation (Fig. 5f) owing to the appreciable concentration of minor tautomer (>10%), which was confirmed by DFT calculations (Supplementary Fig. 13).

Discussion

The three examples reported in this study support a more generalized phenomenon of self-inhibition among tautomeric crystals when growth conditions lead to an appreciable concentration of minor tautomer(s) that function as native inhibitors of crystallization. This mode of action is unique among modifiers reported in literature where the molecular structure and/or composition of an inhibitor typically differs from the solute. Examples include constitutional isomers⁵⁰, stereoisomers¹, tailor-made inhibitors or imposters^{8,46}, and (macro) molecules with similar functional moieties as the solute⁵¹. Here we show that the presence of minor tautomer during crystallization leads to growth cessation under supersaturated conditions. These conditions can be used to tailor crystal properties, such as the rate of dissolution, which is critical for pharmaceuticals. Among the top 200 drugs, there are 33 (including allopurinol) containing tautomers that are prescribed for HIV, epilepsy, COVID-19, schizophrenia, cancer (e.g., skin, lung, and pancreatic), and other diseases that impact millions of people worldwide^{10,12,15}. Minor tautomers also effect other crystal properties, such as elastic moduli that is seemingly related to natural bending. This phenomenon reported here for urate is less frequently reported^{52,53} in comparison to more common examples where malleable crystals bend only under an applied force^{54,55}. The broader relevance of tautomers in crystallization extends to biological systems where the role of natural inhibitors (minor isomers) is elusive. Here we focused on guanine crystals as a representative example owing to their important functional roles in many animals, where these unique properties have also inspired biomimetic engineering of photo/temperature-responsive materials^{17–19,56}. It remains to be determined how the control of major/minor tautomers in natural and synthetic crystals impacts their electronic, magnetic, and/or optical properties.

Methods

Bulk crystallization assays

Ammonium urate (NH₄HU) crystals were synthesized by dissolving appropriate amounts of uric acid sodium salt powder in 20 mL glass scintillation vials containing an aqueous solution of 100 mM NH₄Cl and DI water under rapid agitation at 80 °C. The final solution with a total volume of 15 mL was prepared with equimolar NaHU_(aq) and NH₄Cl_(aq) ranging from 4 to 14 mM. The solution pH (ca. 7) was measured using an Orion Dual Star pH benchtop meter with a ROSS Ultra electrode (8102BNUWP). The sample vials were left undisturbed at 21 ± 1 °C for 24 h to allow crystallization, which was not affected by the presence of NaCl (Supplementary Fig. 15). The crystallization of NH₄HU was also carried out at pH 7 and 11 using the same concentration range without NaCl. In these experiments, the NH₄HU solution was prepared by dissolving appropriate amounts of anhydrous uric acid (UA) powder in 100 mL glass bottles containing DI water and adjusting the pH with 28 wt% ammonium hydroxide (NH₃·H₂O). The crystalline product (in solution) was observed by optical microscopy using a Leica DMI8 instrument. Crystals were also extracted at a periodic time and dried in air overnight. The crystalline phase was analyzed with a Siemens D5000 X-ray diffractometer (XRD) using a Cu K α source (40 kV, 30 mA) and was confirmed by a reference pattern from the solved crystal structure (vide infra). Ex situ microscopy measurements were performed using an FEI 235 dual-beam focused ion beam scanning electron microscopy (SEM). The samples for SEM were coated with ca.

20 nm gold to reduce the effects of electron beam charging. The solubility of NH₄HU crystals at high pH was determined by dispersing purified NH₄HU powder (5–15 mg) in 20 mL vials containing ca. 15 mL of DI water and adjusting the alkalinity (pH 11.0 ± 0.1) with 28% w/w ammonium hydroxide. The vials were sealed with plastic caps and agitated for 24 h at 21 ± 1 °C to accelerate the time to reach solid-liquid phase equilibrium. The identical incubation procedure was repeated for three temperatures (25, 30, and 35 °C). The concentration was monitored over time (5–48 h) to confirm the system reached solid-liquid phase equilibrium. This was accomplished by taking small aliquots of each solution and measuring the UV-Vis absorbance with a Beckman Coulter DU 800 spectrophotometer in a 4 mL quartz cuvette with a 1 cm path length. The concentration was determined using an extinction coefficient of 1.3 ± 0.1 mM⁻¹ cm⁻¹ at a wavelength of 292 nm. Three independent measurements were performed for each temperature and only the average solubility is reported (Supplementary Fig. 4c).

Preparation of NH₄HU crystal seeds

Ammonium urate crystal seeds were prepared in two steps: the spontaneous crystallization from a concentration of 7.5 mM NH₄HU at pH 11; and the transfer of this suspension into 400 mL freshly prepared 5.5 mM NH₄HU growth solution (pH 11) in a 500 mL glass bottle. The NH₄HU solution was prepared by dissolving appropriate amounts of uric acid anhydrous powder in DI water and adjusting the solution to pH 10.2 with 28 wt% ammonium hydroxide (NH₃·H₂O) under rapid agitation at 72 °C. The resultant solution (pH 11) was left at 21 ± 1 °C for 48 h to allow crystallization, and the obtained crystals were transferred into a 5.5 mM NH₄HU growth solution for a 7-day incubation period to produce needle-like crystals of length 10–50 μ m and width <1 μ m. To increase the width of NH₄HU crystals, the product after 7 days of growth was recovered by filtration and the solids were placed into another 5.5 mM NH₄HU growth solution for further incubation. The two-step seeded growth procedure produces crystals with a width of 1–2 μ m.

Structure determination of NH₄HU crystals

Crystal seeds prepared above were too small for structural determination by single-crystal X-ray diffraction; therefore, we obtained structural information from TEM using 3D ED. The NH₄HU crystals were crushed with a mortar and pestle, and then dispersed in pure ethanol. After 5 min of ultrasonication, a droplet of the suspension was transferred onto a copper grid, which was then loaded on a Fischione model 2020 tomography holder. The 3D ED measurements were performed on a Themis Z aberration-corrected electron microscope operated at 300 kV with a 4096 × 4096 Gatan Oneview CMOS camera (15 μ m × 15 μ m pixel size). The microscope is equipped with a monochromator, which was used for adjusting the beam current drawn from the Schottky field-emission electron source. The focus of the monochromator was adjusted to around 200. The microscope was operated in STEM mode during data collection. A quasi-parallel beam was obtained by adjusting the current of the C3 lens until a sharp central spot was observed on the fluorescence screen. The spot size was 10 and the C2 aperture was adjusted to 50 μ m to obtain a quasi-parallel probe with a size of around 200 nm in diameter. The camera length was kept at 185 cm and the highest resolution shell was around 0.85 Å. Additional details of 3D ED data collection and structure determination are provided in Supplementary Section 1.

Powder XRD analysis was used to verify and confirm the structure determination from 3D ED. XRD measurements of NH₄HU crystals were performed at room temperature using a Bruker D8 Advance diffractometer. NH₄HU crystals were loaded into a 0.7 mm borosilicate glass capillary and mounted on the diffractometer operating in a Debye–Scherrer transmission geometry, equipped with Johansson monochromator using Cu K α radiation (λ = 1.5406 Å) and LynxEye

detector, operating at 40 kV and 50 mA. Additional details of crystal structure analysis are provided in Supplementary Section 1.3.

Microfluidic assays

We employed a microfluidic platform described in previous studies^{35,57,58} for in situ analysis of crystal growth kinetics. We tailored the microfluidic device (poly(dimethylsiloxane) on glass) into a cuboid house (ca. 0.5–0.8 mL) where NH₄HU seed crystals landing on the glass substrate were placed in the center (Supplementary Fig. 3c). This system was able to monitor the growth of NH₄HU crystals under continuous supply of fresh growth solution using an inverted optical microscope (Leica DMI8 instrument). Growth solutions prepared with different concentrations (5–12 mM NaHU/NH₄Cl or NH₄HU) and alkalinity (pH 7 or 11) were used in the microfluidics studies. For NH₄HU aqueous solution, an appropriate volume of ammonium hydroxide was added to a suspension of UA powder with pH adjustment. The growth solution was then delivered to the device by a dual syringe pump (CHEMYX Fusion 4000) at a rate of 6 mL h⁻¹ for at least 120 min. The concentration of the growth solution was determined using an extinction coefficient of 1.2 ± 0.1 and 1.3 ± 0.1 mM⁻¹ cm⁻¹ at wavelengths of 290 and 292 nm for neutral and high pH, respectively³². Time-resolved optical micrographs of crystals were analyzed using Image J (NIH)⁵⁹ for quantifying incremental changes in crystal dimension along [010] and [101] directions. The growth rate was measured by linear regression of crystal size over time (e.g., Supplementary Fig. 3g, h). The average growth rates were reported from measurements of 10 to 15 crystals. The flow rate of the growth solution was adjusted to a sufficiently high value to circumvent the influence of diffusion and ensure growth rate measurements were performed in the kinetically-controlled regime (Supplementary Fig. 4a).

Samples for dissolution were prepared on microscope glass slides (Corning) cut to a 9 × 9 mm² size. Glass slides were coated with a thin layer of curable epoxy (Loctite, China) and partially cured in an oven for 2 h at 60 °C prior to sample preparation. Crystals suspended in a saturated solution were mounted on the slide by placing a droplet and allowing 1 h for crystals to settle on the epoxy. The surface was washed with a supersaturated solution (4 mM NH₄HU, pH 7) for 16 h prior to drying at ambient conditions. Microfluidics experiments were performed in DI water (pH 7) and a flow rate of 6 mL h⁻¹ using the same procedure described above.

Analysis of crystal defects

High-resolution TEM observations were performed on the TEAM I electron microscope (NCEM-Molecular Foundry Lawrence Berkeley National Laboratory) by dose fractionation with low-dose rates⁶⁰. In brief, a microscope is operated using a Nelsonian illumination⁶¹, a Cc corrector⁶², and a K2 camera⁶³. The illumination creates a pencil-like, highly-coherent beam of $\Delta E \lesssim 100$ meV that matches the field of view (FoV) of the K2 camera ($\sim 10^7$ Å² at high resolution with an apparent pixel size of 0.3 × 0.3 Å²). This approach allows for the detection of single electron scattering events with dose rates that suppress the degradation of structure information with dose accumulation that is common to radiation-sensitive matter. It also maintains high standards for aberration corrections⁶⁴. See Supplementary Section 1.5 for additional details.

Atomic force microscopy (AFM)

In situ AFM measurements were performed on a Digital Instruments Multimode Nanoscope IV (Santa Barbara, CA) to examine topographical images of NH₄HU crystals and capture the dynamics of (20 $\bar{2}$) surface growth in real-time. NH₄HU crystal seeds (vide supra) were filtered, immobilized on a glass slide (1 × 1 cm²), and mounted on an AFM specimen disk (Ted Pella) by pressing the glass slide to the transfer crystals. AFM images were collected in tapping mode using Olympus BL-AC40TS probes (silicon nitride, Cr/Au coated 5/30,

0.09 N/m spring constant) with a tapping frequency of 30 kHz in a fluid. Image sizes ranged from 300 nm to 1.5 μm with collected using scan rates of 1 to 3 Hz and 256 scan lines at angles depending on the orientation of the monitored crystal^{6,38}. The temperature in the fluid cell (29 °C) reached a steady state value after ca. 20 min imaging, which was confirmed by an AFM kymograph collected with disabled scanning along the y-axis to confirm the solubility.

Growth solutions at different alkalinity (pH 7 and 11) and urate concentrations (2–12 mM) were freshly prepared within 1 h of each measurement. The concentration of growth solutions before use was also measured by UV-Vis spectroscopy with an extinction coefficient of 1.2 ± 0.1 and 1.3 ± 0.1 mM⁻¹ cm⁻¹ at wavelengths of 290 and 292 nm for neutral and high pH, respectively³². The growth solution was continuously delivered to the AFM liquid cell using a dual syringe pump (CHEMYX, Fusion 200). After loading, the solution was left standing for 10–20 min to thermally equilibrate. The crystal edges were first identified in a low-magnification image to determine the orientation and the crystallographic directions. The scan direction was set parallel to the [010] crystallographic direction and AFM images were collected for 3–5 h. For studies of crystal branching at high urate concentration in a neutral solution, we first introduced a slightly supersaturated growth solution (4.0 mM urate) to the AFM liquid cell and allowed the system to reach equilibrium prior to switching to a desired urate concentration. The evolution of NH₄HU crystal surfaces was characterized by the velocity of advancing steps v and the rate of 2D nucleation of new crystal layers J_{2D} , as described in Supplementary Section 1.6.

Contact resonance (CR) AFM was conducted with an Asylum MFP-3D Infinity AFM (Asylum Research, an Oxford Instrument Company, CA) in an ambient environment. Prior to any measurements, the deflection sensitivity of the AFM cantilever (Multi75G, Budget Sensors) was calibrated by force curves on a silicon surface (freshly cleaned by Piranha solution (volume ratio 3:1 for 98% H₂SO₄ and 35% H₂O₂))^{65,66}. The spring constant k_c of the cantilever was calibrated by fitting the first free resonant peak to equations of a simple harmonic oscillator to measure the power spectral density of the thermal noise fluctuations in air^{67,68}. For CR-AFM, the ultrasonic actuation was achieved by gluing the glass substrate (with biomineral crystals on the top surface) to an ultrasonic transducer with a broadband resonance of 2.25 MHz (V133-RM, Olympus NDT)^{65,66,69}. The built-in dual actuation resonance tracking approach of the Asylum MFP-3D AFM was used to track the CR frequency while scanning the sample surface in the straight and bent regions and the total applied force F during the scanning was recorded⁶⁵. The AFM cantilever was modeled as an Euler–Bernoulli beam oscillating with a mechanical constraint at the tip position (see Supplementary Section 1 for details) to extract the tip-sample contact stiffness k^* ^{69–71}. The latter can be converted to the reduced modulus of the tip-sample contact by contact mechanics models. Here, we used the most widely used Hertzian contact model, which approximates the AFM tip-sample contact as a spherical indenter with radius R contacting a flat surface with force F ^{69–71}:

$$k^* = \sqrt[3]{6FRE^*}^2 \quad (1)$$

where E^* is the reduced modulus and is related to the material's elastic property by

$$\frac{1}{E^*} = \frac{1 - \nu_s^2}{E_s} + \frac{1 - \nu_t^2}{E_t} \quad (2)$$

where E_s and E_t are the Young's moduli, and ν_s and ν_t are the Poisson's ratios of the sample and the tip, respectively. The tip position on the cantilever and the tip radius R were calibrated by CR-AFM measurements on a sample with known stiffness (see Supplementary Section 1.7 for more details).

AFM measurements for dissolution were performed in contact mode using a Cypher ES (Asylum Research, Santa Barbara, CA) and silicon nitride probes with a gold reflex coating. Samples were prepared on a glass slide and were attached to specimen disks (Ted Pella) covered with a thin layer of epoxy (Loctite, China). In situ experiments were conducted at ambient temperature by flowing DI water (pH 7) at 6 mL h^{-1} into the liquid cell (ES-Cell-Gas) with a scan rate of 1 Hz at 256 lines per scan.

First-principles calculations

All calculations were performed with the software package Gaussian 09⁷². To obtain accurate geometries and total energies of all possible monovalent and divalent forms of urate tautomers as well as guanine and allopurinol tautomers, we used the complete basis-set, CBS-QB3⁷³, level of theory. Solvation effects were considered by applying the SMD⁷⁴ solvation model with the solvent being water (H₂O). Boltzmann distribution analysis was applied to calculate the population distribution of each possible tautomer at 25 °C using the CBS-QB3 calculated free energies. Density functional theory (DFT) calculations at the M06-2X^{75,76} level of theory with 6-311 + G(d,p) basis set were performed to address the temperature dependence on the urate tautomer population and its effect on the absorption spectra, as well as the kinetics of tautomeric interconversions. The CBS-QB3 and the M06-2X calculations show an excellent agreement in the free energy ranking of the tautomers at room temperature (Supplementary Fig. 19), yielding very similar Boltzmann distributions at room temperature. Vibrational frequency calculations were performed to confirm that each stationary point is either a minimum or a saddle point. Intrinsic reaction coordinate (IRC) calculations⁷⁷ were used to confirm the path connection between the reactant, product, and transition state in tautomer interconversion. Time-dependent DFT was applied at the M06-2X/6-311 + G(d,p) level of theory (same level of theory for the temperature-dependent free energy calculations) to calculate the UV-Vis spectra of monoanionic urate tautomers. Details of the tautomer interconversion reaction calculations are provided in Supplementary Section 1.8.

Spectroscopic verification of urate tautomers

To verify and identify the presence of urate tautomers at neutral solutions, UV-Vis, infrared (IR), and NMR spectroscopies were employed. UV-Vis spectra were recorded on a Beckman Coulter DU 800 spectrophotometer equipped with an external water circulator (Grant LTD6, ± 0.1 °C, United Kingdom) for temperature control. Solutions of NaHU and NH₄HU with a concentration of 1.0 mM were prepared by dissolving known amounts of NaHU in DI water or in equimolar NH₄Cl aqueous solution and DI water at 80 °C. The clear solution of 1.0 mM NaHU was then diluted 20 times to obtain a 0.05 mM solution. These samples have a neutral pH (with values ranging between 7.0 and 7.7). A series of solutions with pH varying from 4.6 (uric acid aqueous solution) to 11.5 with a concentration of 1.0 mM urate were prepared by adjustments with either 1.0 M NaOH_(aq) or 1.0 M HCl_(aq). A stock solution of 1.0 M HCl_(aq) was prepared by adding 8.3 mL of 37% HCl in 100 mL DI water. The UV-Vis spectra of 1.0 mM NaHU, 1.0 mM NH₄HU, and 0.05 mM NaHU were collected at different temperatures, beginning at 10 °C and increasing to 90 °C, and then decreasing from 90 to 30 °C in a 4 mL quartz cuvette of 1 cm path length over a spectral range from 200–400 nm and a scan speed of 120 nm/min (with a wavelength interval of 0.1 nm). The pH of 1.0 mM NaHU at increasing temperatures (21 to 90 °C) was nearly constant (i.e., varying between 7.2 and 6.9).

Fourier transform infrared (FTIR) spectra were recorded on a Thermo Scientific Nicolet 6700 instrument equipped with an Everest Diamond ATR Accessory for solid samples and a Liquid Jacketed Remountable Transmission Liquid Cell (PIKE, USA) for liquid samples. The jacketed transmission cell controlled the temperature of liquids by an external water circulator. A solution

of 18 mM sodium urate in D₂O (instead of H₂O) was prepared to circumvent the significant interferences of broad peaks at 1634 and 3300 cm⁻¹ from the H₂O background. Solution IR spectra were collected at variable temperatures ranging from 10 to 80 °C over a spectral range from 800–4000 cm⁻¹ at a resolution of 2 cm⁻¹. Each spectrum was an average of 128 scans. The solution temperature was controlled by an external water circulator (Thermo Scientific NESLAB RTE-7) with an accuracy of ± 0.1 °C. The solution pH values at different temperatures were also recorded to rule out the influence of pH changes with increasing temperature on urate speciation. Over the range of tested temperatures (22 to 80 °C), the solution pH is approximately constant (i.e. ranging from 7.6 to 7.2); thus, the population of urate monovalent species is >99.0% (Supplementary Fig. 20). For solid samples, IR spectra were collected over a spectral range of 800–4000 cm⁻¹ with the average of 64 scans at a resolution of 2 cm⁻¹.

NMR pH titration experiments were carried out on a 600 MHz JEOL spectrometer equipped with a 5-mm liquids BB probe. NMR samples of 10 mM urate-2-¹³C,1,3,7-¹⁵N₃ labeled solution were prepared by dissolving appropriate amounts of uric acid-2-¹³C,1,3,7-¹⁵N₃ crystal powders in 95% (v/v) H₂O/D₂O containing 0.1% DSS and adjusting the pH by the addition of either 1.0 M HCl_(aq) or 1.0 M NaOH_(aq) as described above. The ¹³C-NMR spectra were acquired with 2048 scans at a free induction decay (FID) resolution of 0.72 Hz; and the ¹⁵N-NMR spectra were acquired with 1024 scans at an FID resolution of 0.46 Hz. For variable-temperature NMR experiments, ¹³C-NMR spectra were collected on an 800 MHz Bruker Avance-III spectrometer equipped with a 5-mm QCI Z-gradient cryo-probe. The temperature was controlled (BVT-3000) with an accuracy of 0.2 °C. The ¹³C-NMR spectra of the 10 mM urate solution (pH 7.6) were acquired by varying the temperatures from 5 to 70 °C with 128 scans at an FID resolution of 0.49 Hz. The ¹³C chemical shifts were determined relative to an internal standard (3-(trimethylsilyl)-1-propane-sulfonic acid sodium salt).

Data availability

Data generated in this study are provided in the Supplementary Information as a Source Data file. The 3D ED and Rietveld refinement coordinates for structures reported in this study have been deposited at the Cambridge Crystallographic Data Centre (CCDC), under deposition numbers 2110687 and 2121918, respectively. These data can be obtained free of charge from The Cambridge Crystallographic Data Centre via www.ccdc.cam.ac.uk/data_request/cif. Source data are provided with this paper.

References

- Orme, C. A. et al. Formation of chiral morphologies through selective binding of amino acids to calcite surface steps. *Nature* **411**, 775–779 (2001).
- Marin, F. & Luquet, G. Molluscan biomineralization: the proteinaceous shell constituents of *Pinna nobilis* L. *Mater. Sci. Eng. C* **25**, 105–111 (2005).
- Porter, S. M. Seawater chemistry and early carbonate biomineralization. *Science* **316**, 1302–1302 (2007).
- Myerson, A. *Handbook of Industrial Crystallization* 2nd edn (Butterworth-Heinemann, 2001).
- Olafson, K. N., Li, R., Alamani, B. G. & Rimer, J. D. Engineering crystal modifiers: bridging classical and nonclassical crystallization. *Chem. Mater.* **28**, 8453–8465 (2016).
- Ma, W., Lutsko, J. F., Rimer, J. D. & Vekilov, P. G. Antagonistic cooperativity between crystal growth modifiers. *Nature* **577**, 497–501 (2020).
- Weissbuch, I., Addadi, L., Lahav, M. & Leiserowitz, L. Molecular recognition at crystal interfaces. *Science* **253**, 637–645 (1991).

8. Addadi, L. et al. Growth and dissolution of organic crystals with “tailor-made” inhibitors—implications in stereochemistry and materials science. *Angew. Chem. Int. Ed. Engl.* **24**, 466–485 (1985).
9. Sangwal, K. *Additives and Crystallization Processes: From Fundamentals to Applications* (John Wiley & Sons, 2007).
10. Katritzky, A. R., Hall, C. D., El-Gendy, B. E.-D. M. & Draghici, B. Tautomerism in drug discovery. *J. Comput. Aided Mol. Des.* **24**, 475–484 (2010).
11. Antonov, L. *Tautomerism: Methods and Theories* (John Wiley & Sons, 2013).
12. Pospisil, P., Ballmer, P., Scapozza, L. & Folkers, G. Tautomerism in computer-aided drug design. *J. Recept. Signal. Transduct.* **23**, 361–371 (2003).
13. Pinsk, N. et al. Biogenic guanine crystals are solid solutions of guanine and other purine metabolites. *J. Am. Chem. Soc.* **144**, 5180–5189 (2022).
14. Gur, D. et al. Guanine crystallization in aqueous solutions enables control over crystal size and polymorphism. *Cryst. Growth Des.* **16**, 4975–4980 (2016).
15. Hernández, B., Luque, F. J. & Orozco, M. Tautomerism of xanthine oxidase substrates hypoxanthine and allopurinol. *J. Org. Chem.* **61**, 5964–5971 (1996).
16. Wang, D. et al. Ketone–enol tautomerism, polymorphism, mechanofluorochromism and solid-state acidochromism of isoquinolinone–arylidenehydrazine derivatives. *J. Mater. Chem. C.* **9**, 12868–12876 (2021).
17. Wu, S.-Q. et al. Macroscopic polarization change via electron transfer in a valence tautomeric cobalt complex. *Nat. Commun.* **11**, 1992 (2020).
18. Sato, O., Cui, A., Matsuda, R., Tao, J. & Hayami, S. Photo-induced valence tautomerism in co complexes. *Acc. Chem. Res.* **40**, 361–369 (2007).
19. Antonov, L. et al. Exploiting tautomerism for switching and signaling. *Angew. Chem. Int. Ed.* **48**, 7875–7878 (2009).
20. Guasch, L. et al. Experimental and chemoinformatics study of tautomerism in a database of commercially available screening samples. *J. Chem. Inf. Model.* **56**, 2149–2161 (2016).
21. Derdour, L. & Skliar, D. A review of the effect of multiple conformers on crystallization from solution and strategies for crystallizing slow inter-converting conformers. *Chem. Eng. Sci.* **106**, 275–292 (2014).
22. Cruz-Cabeza, A. J. & Bernstein, J. Conformational polymorphism. *Chem. Rev.* **114**, 2170–2191 (2014).
23. Raghavan, S. L. et al. Morphology of crystals of α -lactose hydrate grown from aqueous solution. *J. Phys. Chem. B* **104**, 12256–12262 (2000).
24. Dunitz, J. D. & Bernstein, J. Disappearing polymorphs. *Acc. Chem. Res.* **28**, 193–200 (1995).
25. Bernstein, J. & Hagler, A. T. Conformational polymorphism. The influence of crystal structure on molecular conformation. *J. Am. Chem. Soc.* **100**, 673–681 (1978).
26. Yu, L. et al. Thermochemistry and conformational polymorphism of a hexamorphic crystal system. *J. Am. Chem. Soc.* **122**, 585–591 (2000).
27. Eckhardt, C. J. & Bernstein, J. Molecular conformation and electronic structure. Solid-state spectrum of a planar anil. *J. Am. Chem. Soc.* **94**, 3247–3249 (1972).
28. Buttar, D., Charlton, M. H., Docherty, R. & Starbuck, J. Theoretical investigations of conformational aspects of polymorphism. Part 1: o-acetamidobenzamide. *J. Chem. Soc. Perkin Trans. 2*, 763–772 (1998).
29. Derdour, L., Pack, S. K., Skliar, D., Lai, C. J. & Kiang, S. Crystallization from solutions containing multiple conformers: a new modeling approach for solubility and supersaturation. *Chem. Eng. Sci.* **66**, 88–102 (2011).
30. Yoreo, J. J. D. & Vekilov, P. G. Principles of crystal nucleation and growth. *Rev. Mineral. Geochem.* **54**, 57–93 (2003).
31. Smith, C. R. et al. Pathophysiological and physicochemical basis of ammonium urate stone formation in dolphins. *J. Urol.* **192**, 260–266 (2014).
32. Geng, X., Meegan, J., Smith, C., Sakhaee, K. & Rimer, J. D. Crystallization of hierarchical ammonium urate: insight into the formation of cetacean renal stones. *Cryst. Growth Des.* **19**, 6727–6735 (2019).
33. Friedel, P., Bergmann, J., Kleeberg, R. & Schubert, G. A proposition for the structure of ammonium hydrogen (acid) urate from uroliths. *Z. Kristallogr.* **2**, 522 (2006).
34. Kahn, K., Serfozo, P. & Tipton, P. A. Identification of the true product of the urate oxidase reaction. *J. Am. Chem. Soc.* **119**, 5435–5442 (1997).
35. Sosa, R. D., Geng, X., Reynolds, M., Rimer, J. D. & Conrad, J. C. A microfluidic approach for probing hydrodynamic effects in barite scale formation. *Lab Chip* **19**, 1534–1544 (2019).
36. Davey, R. & Garside, J. *From Molecules to Crystallizers* (Oxford Univ. Press, 2000).
37. Le-Bert, C. R. et al. Comparison of potential dietary and urinary risk factors for ammonium urate nephrolithiasis in two bottlenose dolphin (*Tursiops truncatus*) populations. *Am. J. Physiol. Ren. Physiol.* **315**, F231–F237 (2018).
38. Olafson, K. N., Ketchum, M. A., Rimer, J. D. & Vekilov, P. G. Mechanisms of hematin crystallization and inhibition by the anti-malarial drug chloroquine. *Proc. Natl Acad. Sci. USA* **112**, 4946–4951 (2015).
39. Gilmer, G. H., Ghez, R. & Cabrera, N. An analysis of combined surface and volume diffusion processes in crystal growth. *J. Cryst. Growth* **8**, 79–93 (1971).
40. Sleutel, M. & Van Driessche, A. E. S. On the self-purification cascade during crystal growth from solution. *Cryst. Growth Des.* **13**, 688–695 (2013).
41. Davey, R. J., Milisavljevic, B. & Bourne, J. R. Solvent interactions at crystal surfaces: the kinetic story of α -resorcinol. *J. Phys. Chem.* **92**, 2032–2036 (1988).
42. Liu, Y. et al. When crystals do not grow: the growth dead zone. *Cryst. Growth Des.* **19**, 4579–4587 (2019).
43. Markov, I. V. *Crystal Growth for Beginners: Fundamentals of Nucleation, Crystal Growth and Epitaxy* (World Scientific, 2016).
44. Li, D. et al. Tautomerism provides a molecular explanation for the mutagenic properties of the anti-HIV nucleoside 5-aza-5,6-dihydro-2'-deoxycytidine. *Proc. Natl Acad. Sci. USA* **111**, E3252–E3259 (2014).
45. Kolehmainen, E. et al. Substituent and temperature controlled tautomerism: multinuclear magnetic resonance, X-ray, and theoretical studies on 2-phenacylquinolines. *J. Chem. Soc. Perkin Trans. 2*, 1259–1266 (2000).
46. Rimer, J. D. et al. Crystal growth inhibitors for the prevention of L-cystine kidney stones through molecular design. *Science* **330**, 337–341 (2010).
47. Prusiner, P. & Sundaralingam, M. Stereochemistry of nucleic acids and their constituents. XXIX. Crystal and molecular structure of allopurinol, a potent inhibitor of xanthine oxidase. *Acta Crystallogr. B* **28**, 2148–2152 (1972).
48. Gur, D., Palmer, B. A., Weiner, S. & Addadi, L. Light manipulation by guanine crystals in organisms: biogenic scatterers, mirrors, multi-layer reflectors and photonic crystals. *Adv. Funct. Mater.* **27**, 1603514 (2017).
49. Hirsch, A. et al. Biologically controlled morphology and twinning in guanine crystals. *Angew. Chem. Int. Ed.* **129**, 9548–9552 (2017).
50. Chung, J. et al. Factors differentiating the effectiveness of polyprotic acids as inhibitors of calcium oxalate crystallization in kidney stone disease. *Cryst. Growth Des.* **18**, 5617–5627 (2018).

51. Farmanesh, S. et al. Specificity of growth inhibitors and their cooperative effects in calcium oxalate monohydrate crystallization. *J. Am. Chem. Soc.* **136**, 367–376 (2014).
52. Shtukenberg, A. G., Punin, Y. O., Gujral, A. & Kahr, B. Growth actuated bending and twisting of single crystals. *Angew. Chem. Int. Ed.* **53**, 672–699 (2014).
53. Punin, Y. O. & Artamonova, O. I. Autodeformation bending of gypsum crystals grown under the conditions of counterdiffusion. *Crystallogr. Rep.* **46**, 138–143 (2001).
54. Commins, P., Karothu, D. P. & Naumov, P. Is a bent crystal still a single crystal? *Angew. Chem. Int. Ed.* **58**, 10052–10060 (2019).
55. Saha, S., Mishra, M. K., Reddy, C. M. & Desiraju, G. R. From molecules to interactions to crystal engineering: mechanical properties of organic solids. *Acc. Chem. Res.* **51**, 2957–2967 (2018).
56. Leroy, L. et al. Controlled light and temperature induced valence tautomerism in a cobalt-*o*-dioxolene complex. *Inorg. Chem.* **60**, 8665–8671 (2021).
57. Kim, D., Moore, J., McCoy, C. P., Irwin, N. J. & Rimer, J. D. Engaging a battle on two fronts: dual role of polyphosphates as potent inhibitors of struvite nucleation and crystal growth. *Chem. Mater.* **32**, 8672–8682 (2020).
58. Sosa, R. D., Geng, X., Conrad, J. C., Reynolds, M. A. & Rimer, J. D. Suppressing barium sulfate crystallization with hydroxycitrate: a dual nucleation and growth inhibitor. *Chem. Mater.* **33**, 6997–7007 (2021).
59. Rasband, W. S. ImageJ. <http://imagej.nih.gov/ij/> (2011).
60. Kisielowski, C. et al. Modulating electron beam–sample interactions in imaging and diffraction modes by dose fractionation with low dose rates. *Microsc. Microanal.* **27**, 1–11 (2021).
61. Kisielowski, C. On the pressing need to address beam–sample interactions in atomic resolution electron microscopy. *J. Mater. Sci.* **51**, 635–639 (2016).
62. Henderson, R. From electron crystallography to single particle cryoEM (Nobel Lecture). *Angew. Chem. Int. Ed.* **57**, 10804–10825 (2018).
63. Grob, P. et al. Ranking TEM cameras by their response to electron shot noise. *Ultramicroscopy* **133**, 1–7 (2013).
64. Kisielowski, C. et al. Instrumental requirements for the detection of electron beam-induced object excitations at the single atom level in high-resolution transmission electron microscopy. *Micron* **68**, 186–193 (2015).
65. Tu, Q. et al. Quantitative subsurface atomic structure fingerprint for 2D materials and heterostructures by first-principles-calibrated contact-resonance atomic force microscopy. *ACS Nano* **10**, 6491–6500 (2016).
66. Tu, Q. et al. Interfacial mechanical properties of graphene on self-assembled monolayers: experiments and simulations. *ACS Appl. Mater. Interfaces* **9**, 10203–10213 (2017).
67. Hutter, J. L. & Bechhoefer, J. Calibration of atomic-force microscope tips. *Rev. Sci. Instrum.* **64**, 1868–1873 (1993).
68. Walters, D. A. et al. Short cantilevers for atomic force microscopy. *Rev. Sci. Instrum.* **67**, 3583–3590 (1996).
69. Zauscher, S., Parlak, Z. & Tu, Q. in *Handbook of Nanomaterials Properties*. Chapter 31 (eds Bhushan, B., Luo, D., Schrickler, S., Sigmund, W. & Zauscher, S.) (Springer, 2014).
70. Rabe, U. in *Applied Scanning Probe Methods II: Scanning Probe Microscopy Techniques*. Chapter 2 (eds Bhushan, B. & Fuchs, H.) (Springer, 2006).
71. Rabe, U. et al. Quantitative determination of contact stiffness using atomic force acoustic microscopy. *Ultrasonics* **38**, 430–437 (2000).
72. Frisch, M. J. et al. (Gaussian, Inc., 2009).
73. Montgomery, J. A. Jr, Frisch, M. J., Ochterski, J. W. & Petersson, G. A. A complete basis set model chemistry. VI. Use of density functional geometries and frequencies. *J. Chem. Phys.* **110**, 2822–2827 (1999).
74. Marenich, A. V., Cramer, C. J. & Truhlar, D. G. Universal solvation model based on solute electron density and on a continuum model of the solvent defined by the bulk dielectric constant and atomic surface tensions. *J. Phys. Chem. B* **113**, 6378–6396 (2009).
75. Zhao, Y. & Truhlar, D. G. The M06 suite of density functionals for main group thermochemistry, thermochemical kinetics, non-covalent interactions, excited states, and transition elements: two new functionals and systematic testing of four M06-class functionals and 12 other functionals. *Theor. Chem. Acc.* **120**, 215–241 (2008).
76. Zhao, Y. & Truhlar, D. G. A new local density functional for main-group thermochemistry, transition metal bonding, thermochemical kinetics, and noncovalent interactions. *J. Chem. Phys.* **125**, 194101 (2006).
77. Hratchian, H. P. & Schlegel, H. B. Accurate reaction paths using a Hessian based predictor–corrector integrator. *J. Chem. Phys.* **120**, 9918–9924 (2004).

Acknowledgements

J.D.R. acknowledges financial support from the Office of Navy Research (Grant Nos. N00014-21-1-2173 and N00014-20-1-2083) and The Welch Foundation (Grant No. E-1794). G.M. acknowledges financial support from the National Science Foundation (NSF, CBET-CAREER program) under Grant No. 1652694 and computational support from the University of Pittsburgh Center for Research Computing. A.J.F. would like to thank the EPSRC Future Continuous Manufacturing and Advanced Crystallisation Research Hub (Grant No. EP/PO06965/1), ARTICULAR: Artificial Intelligence for Integrated ICT-enabled pharmaceutical manufacturing (Grant No. EP/R032858/1), UKRPIF (UK Research Partnership Fund) award from the Higher Education Funding Council for England (HEFCE) (Grant No. HH13054) for funding this work. X.Z. received financial support from the Swedish research council (Grant Nos. VR 2017-04321 and VR 2019-00815) and the Knut & Alice Wallenberg Foundation (Grant Nos. 2012.0112 and 2018.0237). Electron microscopy is supported by the Molecular Foundry, which is supported by the Office of Science, the Office of Basic Energy Sciences, and the US Department of Energy under Grant No. DE-AC02-05CH11231 (proposal 6225). Q.T. acknowledges the support by the startup funds from the Texas A&M Engineering Experiment Station (TEES). W.T. acknowledges financial support from the National Natural Science Foundation of China (Grant No. NNSFC 22278300). We also thank Dr. Si Li for her help with dissolution measurements and Prof. Junbo Gong for providing access to laboratory facilities.

Author contributions

J.D.R. supervised the project. W.T. performed NH₄HU bulk, microfluidics, and in situ AFM crystallization assays, FTIR and UV-Vis measurements, and prepared samples for additional characterization; X.G. assisted with bulk crystallization assays and sample preparation; W.T. and J.D.R. analyzed and discussed the data. G.M., C.A.M.-R., and S.H. performed first-principles and DFT calculations; T.Y. and X.Z. performed data collection and ab initio structure determination by 3D ED; V.K.S. and A.J.F. collected and analyzed powder XRD for structure refinement; H.M. performed liquid NMR measurements; Q.T. performed AFM nanomechanical characterization; H.A.C., C.K., and F.C.R.H. performed high-resolution TEM measurements. W.T. and X.K. performed the analyses of allopurinol and guanine crystallization; V.P.C. performed ammonium urate dissolution experiments; all authors contributed to the writing and editing of the manuscript.

Competing interests

The authors declare no competing interests.

Additional information

Supplementary information The online version contains supplementary material available at <https://doi.org/10.1038/s41467-023-35924-3>.

Correspondence and requests for materials should be addressed to Jeffrey D. Rimer.

Peer review information *Nature Communications* thanks the anonymous reviewers for their contribution to the peer review of this work. Peer reviewer reports are available.

Reprints and permissions information is available at <http://www.nature.com/reprints>

Publisher's note Springer Nature remains neutral with regard to jurisdictional claims in published maps and institutional affiliations.

Open Access This article is licensed under a Creative Commons Attribution 4.0 International License, which permits use, sharing, adaptation, distribution and reproduction in any medium or format, as long as you give appropriate credit to the original author(s) and the source, provide a link to the Creative Commons license, and indicate if changes were made. The images or other third party material in this article are included in the article's Creative Commons license, unless indicated otherwise in a credit line to the material. If material is not included in the article's Creative Commons license and your intended use is not permitted by statutory regulation or exceeds the permitted use, you will need to obtain permission directly from the copyright holder. To view a copy of this license, visit <http://creativecommons.org/licenses/by/4.0/>.

© The Author(s) 2023